LA-UR-17-30563
Approved for public release; distribution is unlimited.

Title: Design and Simulation of a Planar Micro-Optic Free-Space Receiver

Author(s): Nadler, Brett Ross
Hallas, Justin M.
Karp, Jason H.
Ford, Joseph E.

Intended for: International Optical Design Conference, 2017-07-09/2017-07-13
(Denver, Colorado, United States)

Issued: 2017-11-17

Design and Simulation of a Planar Micro-Optic Free-Space Receiver

Brett R. Nadler*[a], Justin M. Hallas, Jason H. Karp, Joseph E. Ford
University of California San Diego, Department of Electrical and Computer Engineering, 9500 Gilman Drive MC 0407, San Diego, USA, 92093; [a]Currently with Los Alamos National Laboratory, Space Instrument Realization, MS D448, Los Alamos, USA, 87545

ABSTRACT

We propose a compact directional optical receiver for free-space communications, where a microlens array and micro-optic structures selectively couple light from a narrow incidence angle into a thin slab waveguide and then to an edge-mounted detector. A small lateral translation of the lenslet array controls the coupled input angle, enabling the receiver to select the transmitter source direction. We present the optical design and simulation of a 10mm x 10mm aperture receiver using a 30μm thick silicon waveguide able to couple up to 2.5Gbps modulated input to a 10mm x 30μm wide detector.

Keywords: Micro-optical devices, Receiver, Concentrators, Free-space optical communication, Zemax

1. INTRODUCTION

Short link free-space receivers provide digital communications for emergency response, multiple building corporate campuses[1–4], and have been included in recent data center concepts[5]. The inability to provide constant high-power signals because of atmospheric effects such as beam wander and signal attenuation[6,7] limits long range applications, but secure line of sight communications with unmanned vehicles is a new application that can benefit from high-bandwidth and low-power optical communication. Constraints for this emerging application include the need for small physical volume, real-time beam tracking, and sufficient temporal bandwidth for high-resolution video transmission. These constraints are a significant hurdle for a mobile optical receiver due to design tradeoffs between aperture size, tracking, and detector complexity. Consequently, our initial effort was directed towards a large aperture receiver compatible with unmanned vehicle requirements, and capable of directional detection and tracking of incident signals.

Figure 1 shows several options for the optical receiver. The most obvious is a single detector sufficiently large to collect the signal energy, with e.g. a 1 cm^2 aperture (Figure. 1a). However, large area photodiodes do not operate in the GHz regime, and the electronics required to operate an array (e.g. 10 x 10) of small photodiodes would be prohibitive, even assuming the noise level could be sufficiently low in the case of a weak source, especially in the presence of conflicting signals.

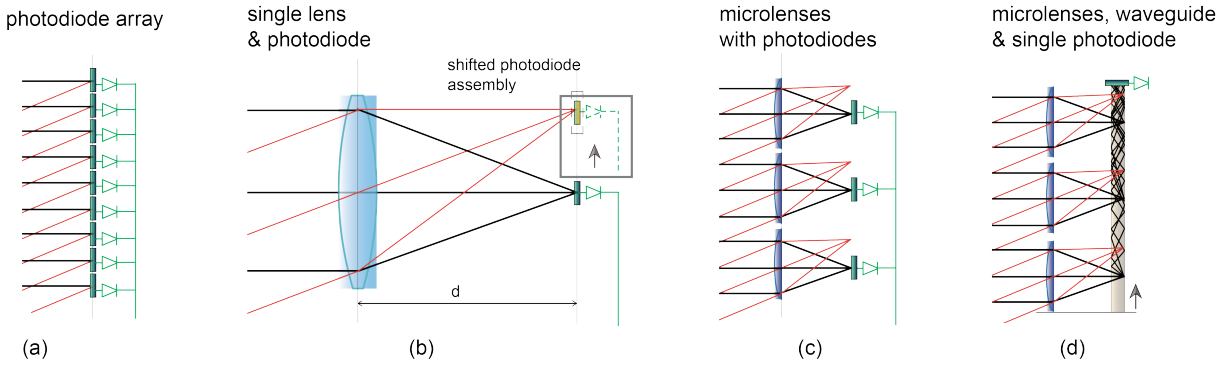

Figure. 1 Typical free-space receiver implementations: (a) array of detectors, (b) bulk optic and a single detector that significantly increases image distance and alignment shift for small field angles, (c) micro-lens array that reduces the number of detectors while introducing alignment shifts, and (d) micro-lens array and waveguide with injection features and an edge detector to reduce number of detectors and image distance.

* Corresponding author: Brett R. Nadler bnadler@lanl.gov, 1-505-667- 5644

A condensing lens such as those found in fixed free space receivers[8–10] concentrate the power of a large aperture onto a single small photodetector, but require active tilting or large lateral shifts of the detector to maintain alignment (Figure. 1b). A range of solutions to this problem has been proposed using multiple lens apertures. An array of shorter focal length micro-lenses, condensing the signal onto a modest number of photodiodes (Figure. 1c) would reduce the lateral shift length for translational alignment, or the tracking might be implemented using micro-electro-mechanical (MEMS) tilt mirrors[11–15]. The signals might be routed directly onto the detectors, or coupled via optical fiber[16]. However, any solution that requires a large matrix of amplified detectors would impose significant complexity and cost, to include electrical power dissipation. Here we propose the alternative configuration shown in Figure. 1d, which is derived from recent research on waveguide-based solar concentrators[17,18]. A micro-lens array and a shared waveguide direct incident light into a detector typically from 50x to 500x smaller than the aperture, and uses a small lateral translation to select and maintain directional alignment.

The most significant design difference between solar and communications concentration is the need to carry time-modulated beams. Our waveguide concentrator homogenizes the input beam and provides disparate optical paths to the detector. This results in a path-dependent delay that limits the temporal bandwidth of the system. For the unmanned vehicle transmission system, we required the transit time through the waveguide to be compatible with a 2.5GHz signal modulation bandwidth, sufficient for high-definition video transmission, and a transmission wavelength of 1550 nm. In the following sections, we explore the concept and formulate software simulations that optimize receiver geometries for these constraints. We conclude that this approach shows promise for a practical directional optical receiver.

2. PLANAR FREE-SPACE RECEIVER CONCEPT

2.1 Waveguide-Based Collection

The micro-optic waveguide concentrator is shown in Figure. 2. Input light is focused by each lens in a lenslet array onto a corresponding array of small reflective facets, micro-optic injection features that couple the reflected light into guided modes of the shared waveguide. The optical signal propagates through the waveguide towards a small exit aperture. The rays exit the waveguide over a range of angles dictated by the injection features and the alignment. A small-area detector is mounted onto the waveguide edge either with direct contact, as shown, or using secondary concentration to further decrease the detector surface area[19].

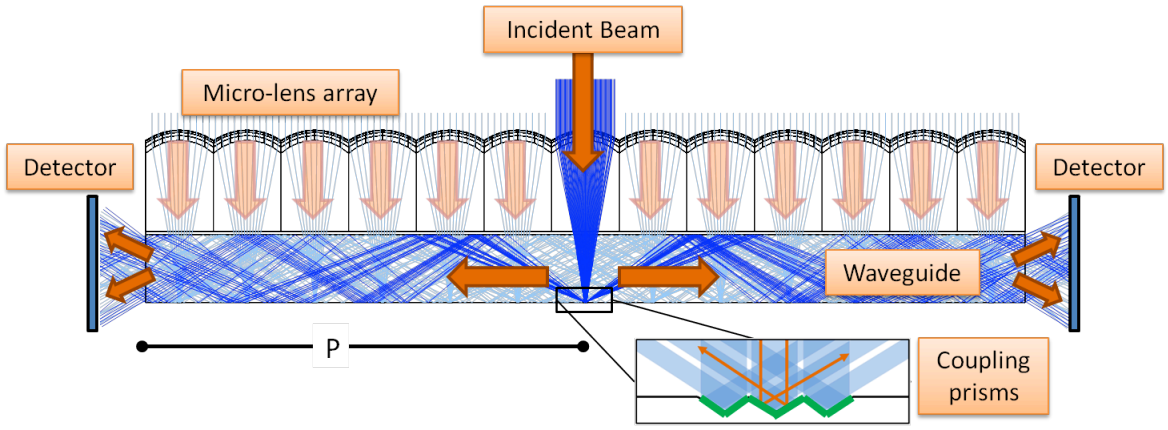

Figure. 2 Receiver diagram showing distribution of incoming light towards the exit aperture of the waveguide using the principle of TIR. The center ray of focused light is reflected by the injection features (prisms in green) located at a position (P) from the edge. Decoupling loss occurs when a ray is incident on adjacent coupling features.

The two primary sources of optical loss in the concentrator are off-axis lens aberrations and focal spot (position) misalignment resulting in poor overlap with the coupler. Fresnel losses and waveguide aberrations such as sag are present however they are minimal over typical waveguide lengths. Once reflected by the couplers, rays guide via total internal reflection (TIR) unless they strike a subsequent prism which strip light from the waveguide. Summing the number of ray and surface interactions, we can calculate theoretical efficiency using the decoupling and positional efficiencies. Total receiver efficiency takes into account the efficiency of the waveguide as well as the detector coupling at the exit aperture.

2.2 Focal Spot Tracking

Conventional concentrator systems employ bulky mechanical trackers to maintain alignment with the sun. Our ability to capture light is different and depends on coupling incident light with the injection prisms on the back of the waveguide. When the focal spots of the incoming light are misaligned with the features, light passes through the waveguide. As a result, translation between the two planar surfaces is adjusted to achieve peak coupling alignment, best performed by optimization. This type of micro-tracking, on the order of the spacing between injection prisms, allows lateral translation to replace conventional tip and tilt[20]. Out-of-plane rotation should not be varied but can be adjusted as a correction for fabrication errors.

The angular separation between incident beams translates to a linear shift of the focal spots on the back of the waveguide defined by,

$$y = 2F/\#\tan\theta_a \tag{1}$$

where θ_a is the acceptance angle of the microlens. This shift decreases the overlapping portions of the focus on the injection feature. When the spot moves a distance y equal to the width of the coupling feature, we achieve complete separation.

2.3 Modal Dispersion

Modal dispersion, the variation in total optical transit time from aperture to detector, dictates the maximum temporal bandwidth for a given waveguide geometry and material. The latency range is defined as the time between the first ray collection and last ray collection by the detector. There will be inter-symbol interference if the power of the first symbol is not removed from the waveguide before subsequent symbols are introduced. Not all power needs to be removed, although residual quantities will decrease the SNR. For our derivation, we assume the absence of optical power contributions from previous symbols. The optical path length (and the distance traveled by the beam) is greatest when reflecting off interfaces at the critical angles θ_c and ϕ_c, a function of the waveguide and gap indices as derived from Snell's Law.

The first TIR is produced at the waveguide and upper gap material interface after the focused beam reflects off the injection feature. When the angle of incidence with the injection feature is sufficiently large the bandwidth limiting value is the critical angle between the waveguide and the edge material, typically air.

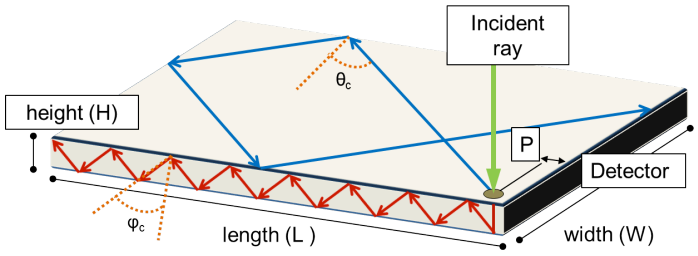

Figure. 3 Longest path starts at a lens closest to the single detector (a). It has a combined vertical and horizontal component through the height (red rays) and length (blue rays) of the waveguide. Path is defined by reflections at critical angles, including the far edge, before returning to the detector. Zemax diagram shows longest path with arbitrary lens and waveguide parameters (b).

As the path laterally traverses the waveguide, the beam undergoes vertical TIR, increasing the optical path length, *pl*, by $1/\sin\phi_c$ where ϕ_c is the minimum critical angle formed between either the gap (above) or surface (below) adjacent to the waveguide. The *pl* through the length of the waveguide is found in a similar manner. For a lateral distance *P* away from the edge the total path length is defined as

$$pl = \frac{P}{\sin\theta_c \sin\phi_c}\ . \tag{2}$$

The maximum modal path length dispersion occurs when the lens array is fully illuminated. The shortest ray path is through the lenslet and corresponding coupling feature nearest the detector. This distance is much less than the longest path and is set to zero for a conservative calculation assuming the case of edge-mounted detectors on opposing sides. The longest path, Figure. 3, is from a coupler adjacent to the detector that injects rays across the length of the waveguide at critical angles with a reflection at the far end, making $P \to 2L$ for a maximum path length of

$$pl_{max} = \frac{2Ln_{wave}^2}{\left(n_{edge}\right)\left(n_{gap}\right)}. \tag{3}$$

The variables n_{wave}, n_{edge}, and n_{gap} represent the index of refraction for the waveguide material, the material around the sides of the waveguide, and the gap material between the lens array and the waveguide, respectively. Using the distance traveled and the speed of the wave within the material, the transit time τ is the inverse of the intersymbol interference-free bandwidth,

$$\tau = c_0 \frac{\left(n_{edge}\right)\left(n_{gap}\right)}{2Ln_{wave}^3}. \tag{4}$$

Instead of the edge reflection, a waveguide can be configured with detectors on each exit aperture. This increases the number of detectors but halves the maximum path length, which doubles the bandwidth. This is the design method we will pursue to achieve high-bandwidth reception.

3. SIMULATION

We created an analytical model of modal dispersion to build basic relationships between receiver geometry, material choice and bandwidth, and implemented those parameters into software. The calculated transit times of individual rays through the model provided an impulse response for the waveguide. Eye diagrams and the Q factor were subsequently derived from the impulse response of the waveguide convolved with digital input signals. We iterated through multiple designs before selecting silicon as the material that would meet bandwidth requirements and provide low loss, high index, and low sag to help with aberrations.

3.1 Optical Design

We used non-sequential ray tracing in Zemax to evaluate microlens, waveguide, and injection feature designs. The selection metric was the maximum optical power throughput, a measure of the receiver efficiency over a number of optimized variables. These included *F/#*, material selection and slab geometries, and injection feature geometry. A large consideration for injection feature size was the effect of off-axis aberrations that enlarge the spot size and decrease the efficiency.

High concentrations and large acceptance angles are obtained with high index lens and waveguide materials, which led to the selection of silicon at η=3.48 for the slab and microlens array. Silicon is transparent at the 1.55μm operating wavelength. Minimizing total detector area and maximizing concentration required waveguide designs that were as thin as possible. We designed for Silicon on Insulator (SOI) material to decouple waveguide thickness from structural requirements, enabling waveguides in the 10μm thickness range. While lens design and injection elements are optimized in the simulation, numerous features were constrained. For example, the 250μm thick lens array substrate and waveguide substrate were chosen to match standard wafer thicknesses, as shown in Figure. 4.

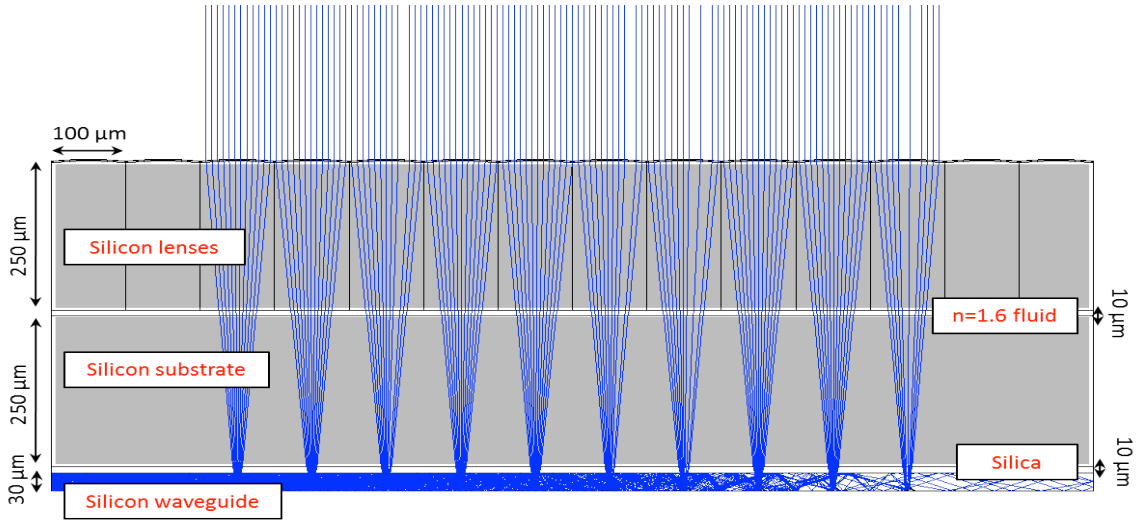

Figure. 4 Layout and ray path for an optimized silicon-based lenslet array and waveguide with n=1.6 index fluid filling the physical gap between the lenses and substrate.

The waveguide substrate is separated from the lens substrate by a gap that can be filled with air or a fluid that is lower in index than the waveguide. The best overall performance was obtained by filling the gap with a relatively high index fluid to minimize geometrical lens aberrations. Various high index materials were evaluated before selecting Cargille Series A optical coupling fluid, n = 1.6, which is a stable liquid with faint yellow coloring. We chose a 10µm thickness for the optical cladding as a reasonable minimum thickness that still supports low waveguide reflection losses.

In compliance with available SOI wafers, we set the waveguide thickness to 30µm with SiO_2 sandwiched between the buried substrate and waveguide to provide wide-angle TIR guiding. We then chose a 10µm spacing of optical coupling fluid at n = 1.46 between the substrate and waveguide. In order to maintain spacing across the gap, 10µm micro-beads were simulated in the fluid. On the bottom of the waveguide, we optimized the injection features to be single central reflective ramps with two symmetric reflective ramps on either side. We can translate the waveguide to maintain alignment with off-axis incident rays.

3.2 Digital Modulation Through Waveguide

The merit function for optimization was based on the total output power coupled to the detector. The variables under consideration were the radius, conic, and aspheric terms of the lenslet array and the position, width, and height of the injection elements. Polarization was allowed and transmission coatings with efficiencies listed at 99.99% were used on surfaces not requiring TIR.

Various waveguide footprints (length and width) were optimized for maximum output power when simulated with an ideal detector at the exit aperture. When we optimized the model, the peak of the symmetric ramps of the prism elements inverted, creating the folded injection feature shown in Figure. 5. This results in an improved efficiency compared to a uniform 60° or 45° prism.[17,21]

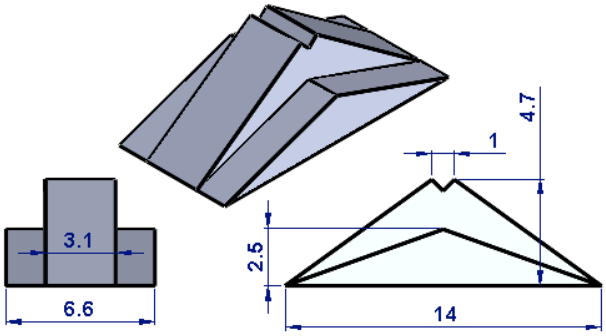

Figure. 5 Optimized injection feature mounted beneath the waveguide. The steep prism with inverted peak is sandwiched between two shallow prisms as measured in microns.

We varied the light source over incident angles θ in a range from -45° to 45° to determine the efficiency of the waveguide at different tracking positions. The resulting calculation of efficiency vs. incident angle is shown in Figure. 6. For our waveguide design with L=10mm, variation in signal loss between ±40° is less than 1.84dB. Asymmetry was noted, somewhat attributable to the bias from a single edge-mounted detector towards the rays directed towards that aperture.

Figure. 6 Maximum simulated efficiency over a range of incident angles.

The most robust option to capture the exiting light is placing a detector in intimate contact with the substrate surface. Since PIN photodiodes decrease in aperture for high bandwidths because of capacitance and transit time limitations, large area detectors are problematic. Unlike fiber optics and their circular high-bandwidth detectors, the exit aperture of the waveguide is rectangular and requires a similarly shaped detector. In addition, the surface area of the edge can be larger than typical off-the-shelf components. While it is not our intent to provide a detailed design of a custom high-bandwidth detector, it is possible to demonstrate that a detector could be fabricated for specific waveguide dimensions and support the designed receiver transmission rates. Models for transit time[22] and capacitance (RC bandwidth)[23,24] for a PIN photodiode illuminated transversely with an InGaAs intrinsic layer are described by

$$t_T = \frac{W}{v_{sat}} \tag{5}$$

where t_T is transit time, W is the width of the depletion region and v_{sat} is the saturation velocity and by

$$f_C = \frac{W}{2\pi\varepsilon_i RA} \tag{6}$$

where f_c is the capacitance bandwidth, ε_i is the permittivity of the InGaAs i-layer, R is the resistance, and A is the active area. The total bandwidth of the detector is found by

$$f_B(W) = \frac{1}{\left(t_T + \frac{1}{f_C}\right)} \tag{7}$$

when $R = 50\Omega$, $v_{sat} = 10^5 m/s$, and $\varepsilon_i = 11.56 * \varepsilon_0$. We found a convergence region that is within the transit and capacitance limits while achieving the proposed bandwidth of 2.5GHz.

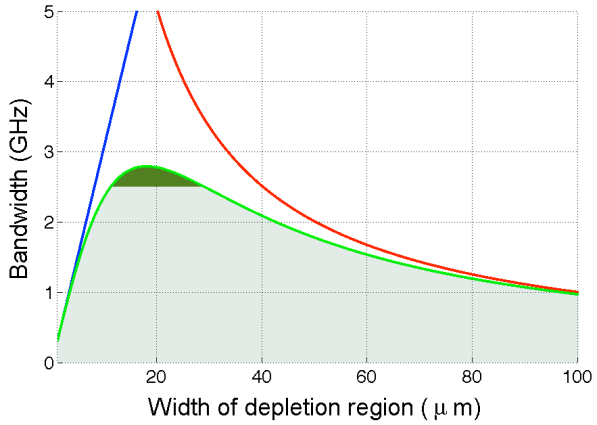

Figure. 7 The total bandwidth (green) is shown as the combination of transit (blue) and capacitance (red) bandwidths. The shaded area above 2.5 GHz corresponds to depletion region widths that are design options for a 0.1mm^2 PIN detector.

The plot in Figure. 7 shows a custom detector that achieves 2.5GHz at 0.1mm^2. Limiting the size of the exit aperture made the detector geometry a constraint in defining the physical system. Exit apertures larger than 0.1mm^2 are accommodated by a series of detectors that appropriately fill the area.

We limited ourselves to three 30μm x 3.33mm ideal detectors to cover the edge of our optimized optical system in a non-sequential Zemax model and used the model to check for the effects of modal dispersion. Ray timing data was generated by sending a full-aperture beam of λ=1552nm rays to be incident on a representative three-dimensional lenslet array. Individual rays were traced as they reflected off the mirrored injection features and propagated through the waveguide. We linked the Zemax model to Matlab analytics using a set of database manipulation scripts that allowed all light ray paths to be imported into a Matlab structure[25]. The first step generated a scatter plot of ray arrival times and their associated intensities as measured by the detector model. Each ray corresponded to a single point on the plot and is delayed from the incident time to the target detector by the optical path length through the waveguide, Figure. 8a. Our second step was to calculate the system impulse response by generating the output light intensity upon the detector as a function of time for a single set of incident rays, Figure. 8b. The shape of the impulse response is a direct result of the different optical paths through the waveguide. A 10-bit PRBS generator convolved with the impulse response provided the equivalent of a received digital signal. The output of the convolution was plotted as an eye diagram.

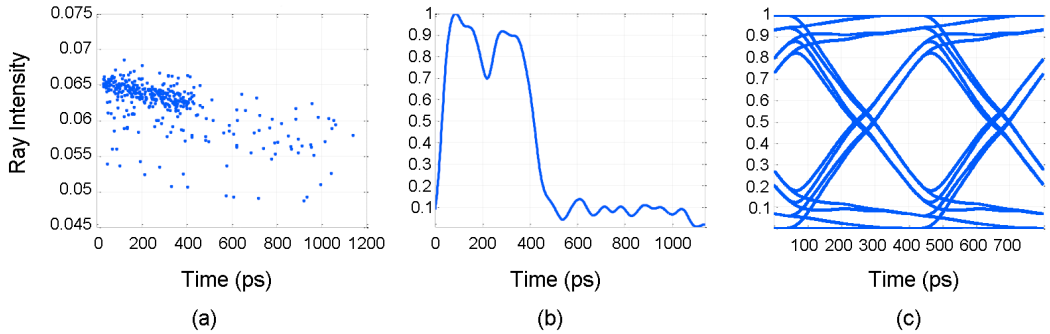

Figure. 8 On-axis incident rays were time stamped with an associated intensity at the detector (a) and compiled into an intensity-based impulse response of the waveguide as a function of time (b). We convolved the impulse response with a 10-bit PRBS signal at 2.5 GHz to yield the simulated system eye diagram m in (c).

These bandwidth analytics were run for the optimized silicon-based system to determine its suitability for telecom implementation. The eye diagram in Figure. 8c was generated using the impulse response of the 10mm per side waveguide convolved with a 2.5 GHz 10-bit PRBS signal.

Our final design with L=10mm and detectors placed on each exit aperture yielded a receiver that functions at 2.5GHz bandwidth. Further reductions in waveguide length or width would increase the bandwidth, in proportion to aperture area.

4. CONCLUSION

In this paper, we present a concept for a lens and waveguide concentrator system that demonstrates a cost effective free-space receiver design for mobile applications. Micro-lens arrays were used to focus incident beam sources onto injection features that couple the light via TIR into the waveguide. The lateral positioning of the prisms determined the amount of reflected light that propagated to the edge and is captured by high-speed detectors. A software model of the concentrator was built and digital PRBS signals were simulated. The model was optimized for geometry, material, and injection shape to pass at least 2.5GHz signals at 1550nm. The resulting silicon lens array, substrate, and waveguide had a 1 cm^2 aperture. Uniquely, the prisms on a waveguide 30µm thick were not uniform. We optimized a solution that sandwiched a 33.9° feature with an inverted peak between two features with shallower angles at 19.7° for maximum light power propagation to the exit apertures.

ACKNOWLEDGMENTS

This work was supported in part by Los Alamos National Security and the National Science Foundation Center for Integrated Access Networks (CIAN).

REFERENCES

[1] V. W. S. Chan, "Free-Space Optical Communications," *Light. Technol. J.* **24**(12), 4750–4762 (2006) [doi:10.1109/JLT.2006.885252].

[2] D. J. T. Heatley, D. R. Wisely, I. Neild, and P. Cochrane, "Optical wireless: the story so far," *IEEE Commun. Mag.* **36**(12), 72–74, 79–82 (1998) [doi:10.1109/35.735881].

[3] J. Moisel, J. Guttmann, H.-P. Huber, O. Krumpholz, M. Rode, R. Bogenberger, and K.-P. Kuhn, "Optical backplanes with integrated polymer waveguides," *Opt. Eng.* **39**(3), 673–679, SPIE (2000) [doi:10.1117/1.602413].

[4] X. Wang, C. Y. Hsu, and X. Jin, "Mobile free space optical communication system," in *Proc. SPIE* **6877**(1), pp. 687706–687706–7, SPIE (2008) [doi:10.1117/12.763275].

[5] H. L. Davidson, J. R. Hamilton, R. A. Hyde, A. Josefsberg, E. K. Y. Jung, J. T. Kare, R. W. Lord, K. Lustig, W. H. Mangione-Smith, et al., "Data center with free-space optical communications," 20110164880, USA (2011).

[6] B. Epple and H. Henniger, "Discussion on design aspects for free-space optical communication terminals," *IEEE Commun. Mag.* **45**(10), 62–69 (2007) [doi:10.1109/MCOM.2007.4342824].
[7] C. C. Davis, I. I. Smolyaninov, and S. D. Milner, "Flexible optical wireless links and networks," *IEEE Commun. Mag.* **41**(3), 51–57 (2003) [doi:10.1109/MCOM.2003.1186545].
[8] fSONA, "SONAbeam® Delivers Broadband Access Through Laser Technology," 2013, <http://www.fsona.com/product.php>.
[9] Lightpointe, "Leader in Low Latency Gigabit capacity point-to-point wireless bridges," 2013, <http://www.lightpointe.com/freespaceoptics.html>.
[10] Canon, "Canobeam: Complete Laser FSO Solutions for Low-Cost, High-Security, High-Speed Data Transmission Networks," 2013, <http://www.usa.canon.com/cusa/professional/products/free_space_optics/data>.
[11] K. Takahashi, H. N. Kwon, M. Mita, K. Saruta, and J. Lee, "A Silicon Micromachined f - theta Microlens Scanner Array by Double-Deck Device Design Technique," *IEEE J. Sel. Top. Quantum Electron.* **13**(2), 277–282 (2007) [doi:10.1109/JSTQE.2007.893099].
[12] Y. Huang, C. Fu, and Q. Bao, "Control Method for High-Accuracy Fine Steering Mirror Based on Slow Sampling Rate of Tracking Sensor Signal," in *Information, Decis. Control*, pp. 78–81 (2007) [doi:10.1109/IDC.2007.374529].
[13] A. Tuantranont, V. M. Bright, J. Zhang, W. Zhang, J. A. Neff, and Y. C. Lee, "Optical beam steering using MEMS-controllable microlens array," *Sensors Actuators A Phys.* **91**(3), 363–372 (2001) [doi:10.1016/S0924-4247(01)00609-4].
[14] K. Hirabayashi, T. Yamamoto, S. Hino, Y. Kohama, and K. Tateno, "Optical beam direction compensating system for board-to-board free space optical interconnection in high-capacity ATM switch," in *Light. Technol. J.* **15**(5), pp. 874–882 (1997) [doi:10.1109/50.580830].
[15] J. Chou, K. Yu, T. Bakhishev, D. Horsley, R. Walmsley, S. Mathai, M. Tan, S.-Y. Wang, V. Subramanian, et al., "Rotational optical alignment for array based free space board-to-board optical interconnect with zero power hold," in *Micro Electro Mech. Syst. (MEMS), 2010 IEEE 23rd Int. Conf.*, pp. 807–810 (2010) [doi:10.1109/MEMSYS.2010.5442283].
[16] A. M. Brown, D. V. Hahn, D. M. Brown, N. W. Rolander, C.-H. Bair, and J. E. Sluz, "Experimental implementation of fiber optic bundle array wide FOV free space optical communications receiver," *Appl. Opt.* **51**(18), 3995, OSA (2012) [doi:10.1364/AO.51.003995].
[17] J. H. Karp, E. J. Tremblay, and J. E. Ford, "Planar micro-optic solar concentrator," *Opt. Express* **18**(2), 1122–1133, OSA (2010) [doi:10.1364/OE.18.001122].
[18] J. M. Hallas, J. H. Karp, E. J. Tremblay, and J. E. Ford, "Lateral translation micro-tracking of planar micro-optic solar concentrator," in *Proc. SPIE* **7769**(1), pp. 776904–776904–7 (2010) [doi:10.1117/12.860980].
[19] J. H. Karp, E. J. Tremblay, J. M. Hallas, and J. E. Ford, "Orthogonal and secondary concentration in planar micro-optic solar collectors," *Opt. Express* **19**(S4), A673, OSA (2011) [doi:10.1364/OE.19.00A673].
[20] J. M. Hallas, K. A. Baker, J. H. Karp, E. J. Tremblay, and J. E. Ford, "Two-axis solar tracking accomplished through small lateral translations," *Appl. Opt.* **51**(25), 6117, OSA (2012) [doi:10.1364/AO.51.006117].
[21] G. Jiang, S. Baig, and M. R. Wang, "Flexible Polymer Waveguides With Integrated Mirrors Fabricated by Soft Lithography for Optical Interconnection," *J. Light. Technol.* **31**(11), 1835–1841, OSA (2013) [doi:10.1109/JLT.2013.2260132].
[22] J. E. Bowers and C. A. Burrus Jr., "Ultrawide-band long-wavelength p-i-n photodetectors," in *Light. Technol. J.* **5**(10), pp. 1339–1350 (1987) [doi:10.1109/JLT.1987.1075419].
[23] P. S. Matavulj, D. M. Gvozdic, and J. B. Radunovic, "The influence of nonstationary carrier transport on the bandwidth of p-i-n photodiode," in *Light. Technol. J.* **15**(12), pp. 2270–2277 (1997) [doi:10.1109/50.643555].
[24] Y.-G. Wey, K. Giboney, J. Bowers, M. Rodwell, P. Silvestre, P. Thiagarajan, and G. Robinson, "110-GHz GaInAs/InP double heterostructure p-i-n photodetectors," in *Light. Technol. J.* **13**(7), pp. 1490–1499 (1995) [doi:10.1109/50.400717].
[25] D. Griffith, "How to Talk to ZEMAX from Matlab," *Zemax User's Knowl. Base*, 2006.